nature communications

Article

https://doi.org/10.1038/s41467-023-39408-2

Robust negative longitudinal magnetoresistance and spin–orbit torque in sputtered Pt_3Sn and $Pt_3Sn_xFe_{1-x}$ topological semimetal

Received: 20 February 2022

Accepted: 13 June 2023

Published online: 12 July 2023

Check for updates

Delin Zhang[1,5] ✉, Wei Jiang[1,5], Hwanhui Yun[2], Onri Jay Benally[1], Thomas Peterson[3], Zach Cresswell[1], Yihong Fan[1], Yang Lv[1], Guichuan Yu[4], Javier Garcia Barriocanal[4], Przemyslaw Wojciech Swatek[1], K. Andre Mkhoyan[2], Tony Low[1] ✉ & Jian-Ping Wang[1,2,3] ✉

Contrary to topological insulators, topological semimetals possess a nontrivial chiral anomaly that leads to negative magnetoresistance and are hosts to both conductive bulk states and topological surface states with intriguing transport properties for spintronics. Here, we fabricate highly-ordered metallic Pt_3Sn and $Pt_3Sn_xFe_{1-x}$ thin films via sputtering technology. Systematic angular dependence (both in-plane and out-of-plane) study of magnetoresistance presents surprisingly robust quadratic and linear negative longitudinal magnetoresistance features for Pt_3Sn and $Pt_3Sn_xFe_{1-x}$, respectively. We attribute the anomalous negative longitudinal magnetoresistance to the type-II Dirac semimetal phase (pristine Pt_3Sn) and/or the formation of tunable Weyl semimetal phases through symmetry breaking processes, such as magnetic-atom doping, as confirmed by first-principles calculations. Furthermore, Pt_3Sn and $Pt_3Sn_xFe_{1-x}$ show the promising performance for facilitating the development of advanced spin-orbit torque devices. These results extend our understanding of chiral anomaly of topological semimetals and can pave the way for exploring novel topological materials for spintronic devices.

Topological materials provide a promising platform for exploring intriguing physics and designing new materials[1–3]. Given the unique chiral topological surface/edge states in topological materials[4–6], they have been proposed to be used to design novel spin-orbit torque (SOT) memory and logic devices with large spin-torque efficiency (θ_{SH})[7–12]. Most notable technological advancements are the demonstration of θ_{SH} >10 with the switching current density (J_c) lower than 10^6 A/cm^2 in sputtered topological insulators at room temperature[10–12]. Most recent efforts, however, have shifted to the exploration of novel topological semimetals, which possess the exotic physics of the topological bulk states with conduction and valence bands touching at points (WSM/DSM) or lines (nodal line semimetals)[6,13–16], which could benefit more energy-efficient and industry-compatible SOT memory and logic devices. Recently, a relatively large θ_{SH} and SOT magnetization switching through several topological semimetals have indeed been experimentally demonstrated[17–24], hence ushering in their exploration for topological spintronic applications.

[1]Department of Electrical and Computer Engineering, University of Minnesota, Minneapolis, MN 55455, USA. [2]Department of Chemical Engineering and Materials Science, University of Minnesota, Minneapolis, MN 55455, USA. [3]School of Physics and Astronomy, University of Minnesota, Minneapolis, MN 55455, USA. [4]Characterization Facility, University of Minnesota, Minneapolis, MN 55455, USA. [5]These authors contributed equally: Delin Zhang, Wei Jiang.
✉e-mail: dlzhang@umn.edu; tlow@umn.edu; jpwang@umn.edu

One of the most intriguing transport phenomena in topological semimetals is the chiral (Adler-Bell-Jackiw) anomaly, which predicts the transfer of Weyl Fermions with opposite chirality in the presence of parallel electric and magnetic fields[13–16,25–28]. Negative longitudinal magnetoresistance (NLMR) is one of the manifestations of chiral anomaly and commonly considered as an experimental signature of topological semimetals[29–34], as reported in Na_3Bi[13,27], TaAs[14–16], WTe_2[35], $ZrTe_5$[36], Cd_3As_2[37,38], TaP[39], among many others. However, the exact origin of NLMR is still an open debate as there are alternative thin film material systems showing NLMR absence of chiral anomaly, such as topological insulators or disordered semiconductors, whose origin are attributed to Berry curvature induced anomalous velocity and its derivative orbital moment or Zeeman effect on percolating current pathways in disordered bulk[40–46].

Recent theoretical works also predict a linear NLMR in time-reversal symmetry (TRS) breaking WSM instead of quadratic NLMR in the TRS counterpart based on Onsager's relations, where electric current depends linearly on the magnetization[31–33]. Contrary to typical magneto-transport experiments, the NLMR associated with chiral anomaly in a thin film semimetal relies only on the in-plane magnetic field. This effect should be accompanied by additional contributions of the conventional positive magnetoresistance (MR) due to carrier localization induced by the out-of-plane magnetic field. Systematic angle dependent (both in-plane azimuthal and out-of-plane polar angles) magneto-transport study of topological semimetals with/without TRS breaking would allow us to validate and reconcile these different contributions.

Recently, binary Pt-Sn alloys have been identified as a new family of topological materials, which have five known stable phases of different compositions that show rich topological properties. Besides the $PtSn_4$ single crystal, which has already been demonstrated experimentally to be a nodal line Dirac semimetal[47], a more interesting Pt_3Sn alloy has been predicted theoretically to be a promising three-dimensional weak topological insulator hosting type-II Dirac fermion[48]. However, there is no experimental investigation of its topological properties and application in spintronic devices to-date. Meanwhile, fabrication process of a high-ordered and industrial-compatible Pt_3Sn is less challenging compared to some topological materials (e.g. Bi_2Se_3[10] and WTe_2[20,23]).

In this work, we successfully fabricate highly ordered Pt_3Sn with/without seed layers and Fe-doped Pt_3Sn ($Pt_3Sn_xFe_{1-x}$) thin films through sputtering deposition that provides seamless integration with the industry development of memory and logic devices for CMOS technology integration. The Pt_3Sn with/without seed layers and $Pt_3Sn_xFe_{1-x}$ samples show a surprising robust quadratic and linear NLMR, respectively. These results are consistent with the topological semimetal phases of the Pt_3Sn and $Pt_3Sn_xFe_{1-x}$ samples with and without TRS, respectively, which is further corroborated by our DFT calculations. Meanwhile, both azimuthal and polar angular sweepings of the magnetic field reveal a NLMR behavior that is commensurate with the phenomenon of chiral anomaly and can be reliably reproduced within a simple model. Furthermore, we calculate the spin Hall conductivity to be ~$4.34 \times 10^5\ \hbar/2e\ (\Omega \cdot m)^{-1}$ for Pt_3Sn, which is two times larger than that of DSM $PtTe_2$ ($0.2–2 \times 10^5\ \hbar/2e\ (\Omega \cdot m)^{-1}$) and WSM WTe_2 ($2.04 \times 10^5\ \hbar/2e\ (\Omega \cdot m)^{-1}$)[21,49]. θ_{SH} of the Pt_3Sn and $Pt_3Sn_xFe_{1-x}$ thin films is evaluated to be ~ 0.4 and 0.38, respectively, as characterized by spin-torque ferromagnetic resonance (ST-FMR) measurement, which is several times larger than that of $PtTe_2$ (~0.1)[21] and WTe_2 (~0.2)[19] with the same thickness.

Results

Crystalline structure of Pt_3Sn and $Pt_3Sn_xFe_{1-x}$

The crystallinity and microstructure are investigated for the Pt_3Sn, $Pt_3Sn_xFe_{1-x}$, Pt-seeded Pt_3Sn, and Mo-seeded Pt_3Sn thin films deposited on (001) single-crystal MgO substrates with substrate heating at 350 °C. Figure 1a shows the crystalline structure of Pt_3Sn and $Pt_3Sn_xFe_{1-x}$ samples by x-ray diffraction (XRD). We can clearly observe the (111) textured growth for Pt_3Sn and $Pt_3Sn_xFe_{1-x}$ samples with the (111) peak, which is like the Pt reference sample on MgO substrate. We also observe a small (002) peak for both samples, indicating that these

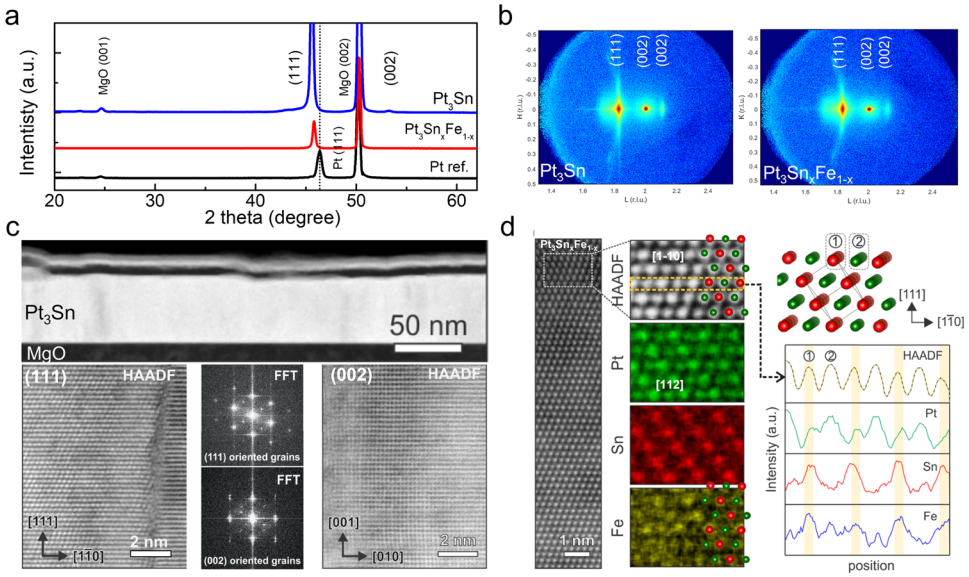

Fig. 1 | Crystalline structure of the Pt_3Sn samples. a Specular (θ–2θ scans) XRD patterns of the Pt reference, Pt_3Sn and $Pt_3Sn_xFe_{1-x}$ thin films. **b** Reciprocal space maps (RSM) around the (002) Bragg reflection of the MgO substrate of the Pt_3Sn and $Pt_3Sn_xFe_{1-x}$ thin films. Both the Pt reference and the Pt_3Sn and $Pt_3Sn_xFe_{1-x}$ thin films grow epitaxially on the MgO substrate along the (111) direction. The XRD experiments show a small amount of (001) oriented grains. **c** HAADF-STEM images of the Pt_3Sn thin film on the MgO substrate. Low-magnification image (top panel) shows the Pt_3Sn film and capping layers with relatively uniform thicknesses. Atomic-resolution HAADF-STEM images obtained from (111) oriented (bottom-left) and (002) oriented (bottom-right) grains demonstrate their crystalline orientations. Fast Fourier transforms (FFTs) from the (111) and (002) oriented grains are also displayed (bottom-middle). **d** Atomic-resolution HAADF-STEM image and EDX elemental maps of the $Pt_3Sn_xFe_{1-x}$. Schematic of the atomic structure is illustrated along with elemental line profiles, extracted from the region in the yellow-dashed line on the HAADF-STEM image.

https://doi.org/10.1038/s41467-023-39408-2

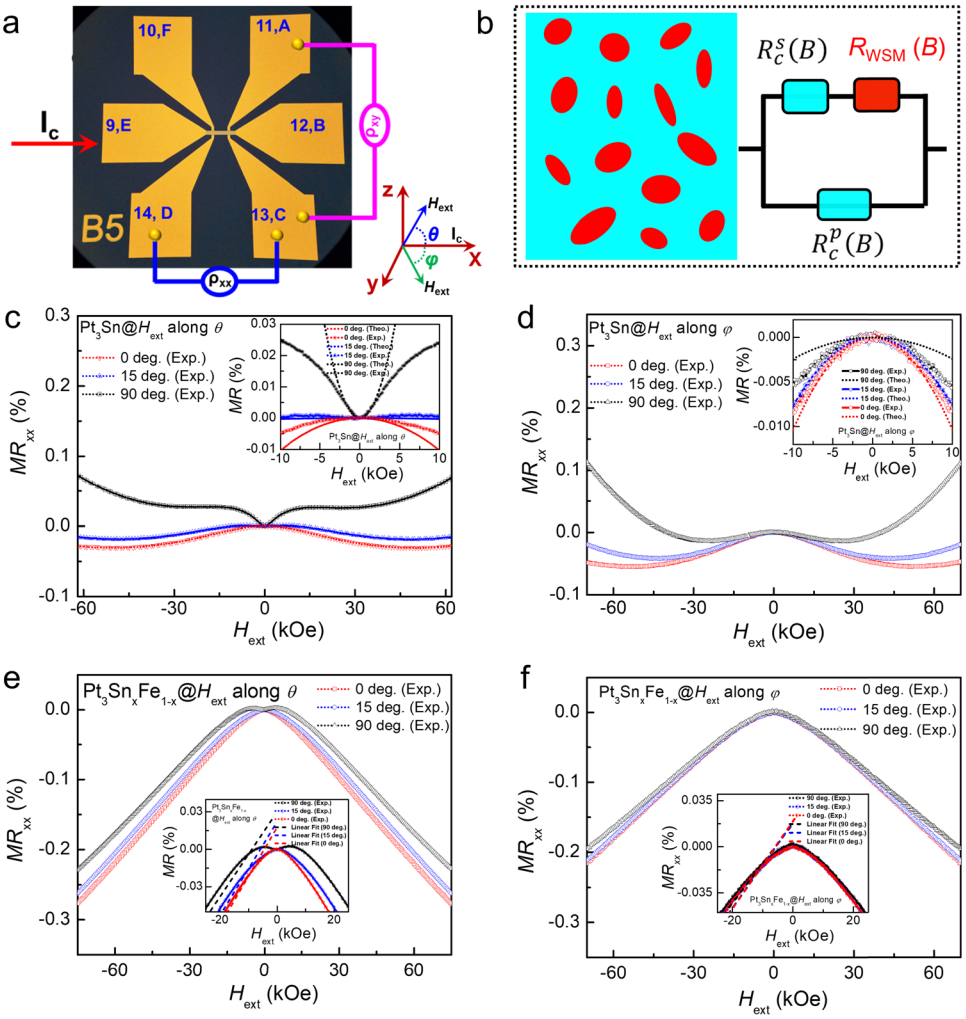

Fig. 2 | Characterization and physical origin of robust NLMR. a The photo image of Hall bar devices used for electric-transport measurements. Where the current (I_c) is applied along x-axis, the external magnetic field (H_{ext}) rotates along *xz* plane with angle θ [out-of-plane magnetoresistance (MR_{xx})] and *xy* plane with angle φ (in-plane MR_{xx}), respectively. **b** Schematic of three-resistor model with conventional resistor (color blue) each connected in series (R_c^s) and in parallel (R_c^p) with the topological semimetal R_{SM} (color red). The red areas represent contributions from topological semimetal (both DSM and WSM) and the blue areas denote normal metallic contribution**. c, d** The experimental measured and theoretically-fitted MR_{xx} vs. H_{ext} curves of Pt_3Sn for θ-angle dependence and φ-angle dependence, respectively. The theoretically-fitted MR_{xx} vs. H_{ext} curves based on three-resistor model are shown in the insert of **c**, **d**. **e**, **f** The experimental measured and theoretically-fitted MR_{xx} vs. H_{ext} curves of $Pt_3Sn_xFe_{1-x}$ for θ-angle dependence and φ-angle dependence, respectively. The theoretically-fitted MR_{xx} vs. H_{ext} curves based on three-resistor model are shown in the insert of **e**, **f**.

Pt_3Sn thin films have (002) orientated grains only in some regions while the dominant texture is along the (111) direction. To further confirm the crystalline orientation, we carried out reciprocal space mapping (RSM) measurements, in units of the MgO lattice (4.212 Å), by XRD, as shown in Fig. 1b. Both (111) and (002) diffraction patterns can be seen for Pt_3Sn and $Pt_3Sn_xFe_{1-x}$ samples, confirming high-ordered phase. For Pt_3Sn thin films with seed layers, Pt seed layer can maintain the (111) texture with certain (002) orientated grains, the same as Pt_3Sn and $Pt_3Sn_xFe_{1-x}$. However, a Mo seed layer induces the (002) texture, as shown in Fig. S1a, b in Supplemental Information (SI). To further investigate the microstructure and chemical composition of the samples, scanning transmission electron microscopy (STEM) measurements were conducted for Pt_3Sn, $Pt_3Sn_xFe_{1-x}$, and Mo-seeded Pt_3Sn samples (Figs. 1c, d, and S2). From the atomic-resolution STEM images, it was confirmed that both Pt_3Sn and $Pt_3Sn_xFe_{1-x}$ samples show primarily (111) textured grains with in-plane twist between them as well as some grains with a (002) texture (Fig. 1c). Mo-seeded Pt_3Sn sample exhibits only (002) growth (see Fig. S2 for details). STEM-energy dispersive X-ray (EDX) analysis was performed (Fig. 1d). Atomic-resolution EDX elemental maps show that the atomic positions of Sn and Fe are overlapping, which directly demonstrates that the Fe atoms are located at the Sn sites. The Fe atoms substituting Sn atoms is also evidenced from comparison of two EDX spectra from $Pt_3Sn_xFe_{1-x}$ and Pt_3Sn samples (see Fig. S2b), where a relative increase of Fe *K* peaks and decrease of Sn *L* peaks in $Pt_3Sn_xFe_{1-x}$ can be seen.

Robust negative magnetoresistance of Pt_3Sn and $Pt_3Sn_xFe_{1-x}$

To investigate the topological properties, the Pt_3Sn and $Pt_3Sn_xFe_{1-x}$ samples were patterned into Hall bar devices with 12-μm width and 144-μm length by using an optical lithography process. The electric-transport properties were tested by a physical property measurement system, as illustrated in Fig. 2a. The resistivity (ρ_{xx}) is measured and calculated to be 162 μΩ.cm and 114 μΩ.cm for Pt_3Sn and $Pt_3Sn_xFe_{1-x}$ at room temperature, respectively (see Fig. S3a in SI). With decreasing temperature, ρ_{xx} exhibits a metallic behavior, reaching at 1.9 K a residual value ρ_0 of ~83 μΩ.cm and 79 μΩ.cm for Pt_3Sn and $Pt_3Sn_xFe_{1-x}$, respectively, due to carrier scattering with impurities or lattice defects. The residual resistivity ratio RRR = ρ(300 K)/ρ(0) ~ 1–2 signals high

quality of the studied thin film materials. Meanwhile, the magnetoresistance (MR_{xx}) vs. external magnetic field (H_{ext}) and Hall resistivity (R_{xy}) vs. H_{ext} of these Pt_3Sn and $Pt_3Sn_xFe_{1-x}$ Hall bar devices were measured at 1.9 K for different angles θ and φ [θ represents the out-of-plane polar angle between H_{ext} and the z-axis; φ denotes the in-plane azimuthal angle between H_{ext} and the x-axis (see Fig. 2a) where the electric current (I_c) is applied along the x-axis], as plotted in Fig. 2c–f. As shown in Fig. 2c, we can clearly see that the measured MR_{xx} is surprisingly negative when $\theta < 15°$ and becomes positive while $\theta > 15°$ for the Pt_3Sn Hall bar device with a wide range of H_{ext}.

This behavior can be ascribed to the presence of at least two competing contributions, whose strength is associated with the polar angle θ between I_c and H_{ext}. Positive contribution of MR is commonly observed in metallic systems that depend only on out-of-plane H_{ext}, which can be easily understood from the electron localization induced by magnetic cyclotron orbits[50]. On the other hand, negative contribution of MR in 2-dimentional electron gas (2DEG) metallic system is rare, albeit only observed in semiconductor system[41,42]. We note that there exist various explanations for the NMR effect, such as the suppression of spin fluctuation under H_{ext}, or the weak localization effect, however, most of those effects cannot explain the experimentally observed angle dependence of the NMR (more discussion in Supplementary Note 3). A defining characteristic of the chiral anomaly in topological semimetals is that it only relies on the magnetic field component parallel to the applied electric field ($H_{ext} \parallel I_c$)[29,51]. To distinguish the contribution between these two components, we further measured MR_{xx} of the Pt_3Sn Hall bar devices with in-plane rotating H_{ext} with different φ, as plotted in Fig. 2d. We can clearly observe NLMR for all azimuthal angles φ whose magnitude decreases when φ changes from 0 degree to 90 degree. Such robust NLMR phenomenon unequivocally confirms the anomaly contribution from the topological semimetal.

To further investigate the intriguing phenomena of Pt_3Sn system, we tested the transport properties of Pt-seeded Pt_3Sn and Mo-seeded Pt_3Sn that possess different orientation with high crystallinity, as shown in Fig. S3b–e. Pt-seeded Pt_3Sn and Mo-seeded Pt_3Sn have similar nontrivial NLMR behavior as that of Pt_3Sn without a seed layer. There is only a slight shape difference in the MR_{xx} curve among Pt_3Sn samples, which can be attributed to sample variations such as doping or crystallinity. It is rather enthralling to observe such robust NLMR in our Pt_3Sn thin films regardless of their different orientations with/without seed layers, strongly suggesting the existence of robust topological semimetal states.

Meanwhile, we also investigated the topological properties of Pt_3Sn doped by magnetic element ($Pt_3Sn_xFe_{1-x}$). With a small amount of Fe dopant (3.8%), $Pt_3Sn_xFe_{1-x}$ presents weak ferromagnetic properties below 25 K (see Supplementary Note 2 and Fig. S4 in SI). Surprisingly, the MR measurement of $Pt_3Sn_xFe_{1-x}$ with rotating H_{ext} (both θ and φ) reveals a very different behavior compared to Pt_3Sn. As summarized in Fig. 2e, f, we observe a nearly angle-independent negative MR phenomenon with a clear linear H_{ext} dependence. The negative MR shows the linear behavior within the applied H_{ext}, which could potentially become non-linear when the magnetic field is larger[52]. Unlike positive linear MR that is more commonly observed, linear NLMR has been proposed for WSMs with broken TRS[31–33], see more discussion in SI. In addition, the results of zoomed-in MR_{xx} vs. H_{ext} curves and Hall resistance (R_{xy}) vs. H_{ext} curves measured at 1.9 K are presented in Fig. S5, in which the weak anti-localization behavior is clearly observed for these Pt_3Sn and $Pt_3Sn_xFe_{1-x}$ samples. Furthermore, the Pt_3Sn samples show the typical Hall Effect, except for $Pt_3Sn_xFe_{1-x}$ with the anomalous contribution, which can be associated to anomalous Hall effect (AHE) (see Fig. S5e–i). The AHE of $Pt_3Sn_xFe_{1-x}$ can be related to a spin-split band structure due to magnetic dopants, and thus further supports the presence of topologically nontrivial electronic structure in our materials.

Physical origin of robust NLMR

To better understand the robust NLMR phenomena observed in Pt_3Sn and $Pt_3Sn_xFe_{1-x}$, a three-resistor model is applied to fit the measured MR results as shown in Fig. 2b. The resistance of trivial metallic state can be well described by the Drude model $R_c(H_{ext}) = R_{c,0}[1 + \alpha(H_{ext} \cdot sin(\theta))^2]$, contributing to positive MR when $H_{ext} \perp I_c$. While that of the topological semimetal states is assumed to be $R_{SM}(H_{ext}) = R_{SM,0}[1 + \beta(H_{ext} \cdot \cos(\theta)\cos(\varphi))^2]$, inducing negative MR for $H_{ext} \parallel I_c$ (see details in Supplementary Note 3 and Fig. S6). $R_{c,0}$ and $R_{SM,0}$ represent the initial resistance without H_{ext}, which can be extracted from experimental measurements. The total resistance can be simplified using a three-resistor model with one conventional resistor each connected in series and in parallel with R_{SM} that is described as $R(H_{ext}) = 1/[\frac{1}{(R_{SM}+R_c^s)} + \frac{1}{R_c^p}]$[45]. We can easily see that with the increase of R_{SM}, the system has higher tendency to yield negative MR (Fig. S7a), while with the increase of either R_c^s or R_c^p, the total MR tends to be more positive (Fig. S7a, c).

This model captures the experimental φ-dependent MR feature of Pt_3Sn. For the in-plane φ-dependent measurement, there will be only contributions from R_{SM}, whose sign remains negative but magnitude changes with the angle between I_c and H_{ext}, as shown in the insert of Figs. 2c, d and S8. However, unlike the ideal theoretical model, the experimental MR does not disappear even for $H_{ext} \perp I_c$, possibly due to the polycrystalline nature of the sputtered Pt_3Sn that hosts various pairs of Weyl fermions along different directions. Additionally, certain weak localization and weak anti-localization effects, that may cause the deviation between theory and experiments, are not considered. Contrary to Pt_3Sn, $Pt_3Sn_xFe_{1-x}$ exhibits almost angle-independent linear negative MR behavior (shown in Fig. 2e, f). Such distinction is possibly related to the distinct nature of the Weyl nodes of TRS-broken WSMs. In time reversal topological semimetal systems, the Weyl pairs are oriented along certain spatial orientations, while the Weyl pairs are locked to H_{ext} in TRS-broken WSMs (see Supplementary Note 4 in SI).

Meanwhile, $Pt_3Sn_xFe_{1-x}$ sample shows relatively low crystal quality that have different crystalline orientations, as suggested from Figs. 1a and S2b. Hence, we attribute the azimuthal angle independence to the random crystalline orientations. On the other hand, linear NLMR has indeed been predicted for TRS-broken WSMs when the type-I Weyl nodes are further tilted to form a one-dimensional chiral anomaly[31–33], which agrees with our DFT calculations (see Supplementary Note 4 in SI). Therefore, we fitted the experimental results using a linear model $MR \cong \alpha + \beta H_{ext}$, which perfectly reproduces experimental results, as shown in the insert of Fig. 2e, f (see details in Supplementary Note 3).

To explore the physical origin of the NLMR behavior, we carried out first-principles calculations of Pt_3Sn and $Pt_3Sn_xFe_{1-x}$ (see Figs. 3a, d for corresponding crystalline structures). The band structure of pristine Pt_3Sn is shown in Fig. 3b. For the pristine phase without SOC, Dirac nodes can be clearly seen at Γ and R points, which become completely gapped when considering SOC, suggesting the topological insulator phase, as also confirmed from our topological edge state calculations (see Fig. S9 in SI). Note that though Pt_3Sn has features of topological insulators, there is a type-II Dirac node and significant bulk states appearing near the Fermi level around R point (Fig. 3c), leading to the formation of a "weak topological insulator" (WTI) or topological semimetal[48]. The coexistence of topological surface states, Dirac fermion, and metallic bulk states in Pt_3Sn constitutes a physical picture as it is consistent with our previous analysis of the competing contributions to MR that are associated with the angle between electric current and magnetic field. The Dirac fermions contribute to the NLMR due to chiral anomaly while the metallic bulk states contribute to positive MR. It is important to mention that although the Dirac node is not located exactly at the Fermi level, theories have demonstrated that NLMR is robust despite departure from the ideal semimetal systems[34].

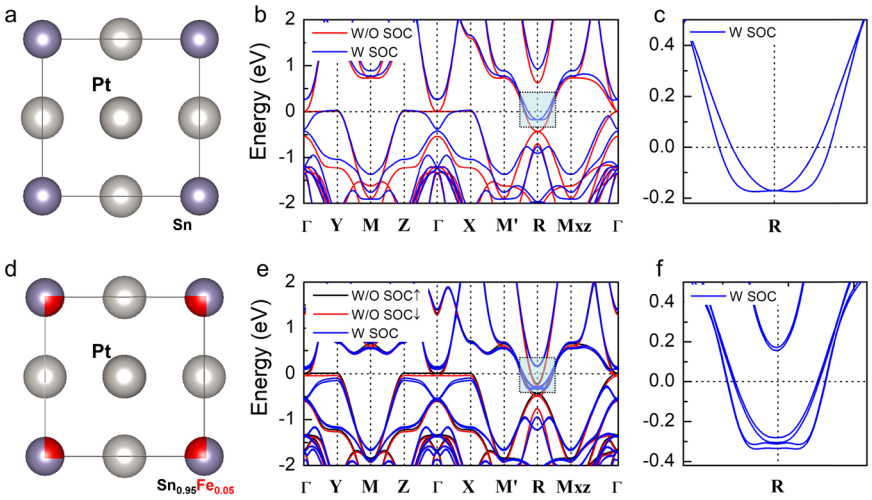

Fig. 3 | Theoretical calculation of topological properties. a, **b** The crystal structure of pristine Pt_3Sn and the band structure of pristine Pt_3Sn that shows weak topological features. Blue and red lines represent band structures with and without spin–orbit coupling, respectively. **c** Enlarged band structure with the Dirac nodes around the R point. **d**, **e** The crystal structure of pristine $Pt_3Sn_xFe_{1-x}$ and its band structure that shows clear spin-splitting and formation of TRS-broken WSM. Blue, black (spin up), and red (spin down) lines represent band structures with/without spin–orbit coupling, respectively. **f** Enlarged band structure with the Weyl nodes around the R point that shows formation of TRS-broken WSM.

The calculated band structure of $Pt_3Sn_xFe_{1-x}$ in the TRS-broken scenario is shown in Fig. 3e. The band structure without SOC shows a clear spin-splitting due to magnetic doping with each spin channel [spin up (black curve) and spin down (red curve)] hosting a set of bands identical to that of pristine Pt_3Sn. When SOC effect is considered, one can clearly see the formation of various pairs of Weyl nodes near the R (Fig. 3f) and Γ points, confirming the formation of TRS-broken WSM phase. Therefore, we have established the topological transition between topological Dirac semimetal and WSM through time-reversal symmetry breaking for the Pt_3Sn and demonstrate the robustness of topological semimetal states against magnetic doping. Considering the possibility of small perturbations of strain or structural defects due to lattice mismatch during sputtering using various seed layers, we also calculated Pt_3Sn with different structural variations, which shows the robustness of topological semimetal states against structural perturbation (see Supplementary Note 4 and Fig. S10 in SI).

Spin torque efficiency (θ_{SH})

After confirming the topological features, we investigate θ_{SH} of the Pt_3Sn and $Pt_3Sn_xFe_{1-x}$ samples utilizing the ST-FMR technique[53,54]. The schematic of the sample stack and testing configuration are illustrated in Fig. 4a, b. To precisely evaluate the spin torque efficiency, we fix the thickness of the Pt_3Sn layer and change the thickness of the CoFeB layer (t_{CoFeB} = 3.0–6.0 nm). Figure 4c, d show the room-temperature ST-FMR spectra of Pt_3Sn (10.0 nm)/CoFeB (5.0 nm) and $Pt_3Sn_xFe_{1-x}$ (10.0 nm)/CoFeB (5.0 nm) devices, respectively, excited at microwave frequency of 9 GHz. The experimental data (black) is fitted to separate the contribution of symmetric Lorentzian (blue) and antisymmetric Lorentzian (pink) curves. The $(\tau_{FL}+\tau_{Oe})/\tau_{DL}$ vs. t_{CoFeB} is plotted in Fig. 4e, f for Pt_3Sn and $Pt_3Sn_xFe_{1-x}$, respectively, where the slope contains the information for damping-like torque (τ_{DL}), the intercept contains the information for field-like torque (τ_{FL}) and the Oersted field contribution (τ_{Oe}, see Supplementary Note 5).

The thickness-dependent measurement estimates the θ_{SH} more reliably by determining the slope of the $(\tau_{FL}+\tau_{Oe})/\tau_{DL}$ ratio over film thickness in Fig. 4e, f, as shown by equation $\frac{J_s}{J_c}=\frac{e\mu_0 M_s}{\hbar}\times\frac{\tau_{AD}}{\tau_{Oe}/(t_{CoFeB}d_{Pt_3Sn})}$[53]. From linear curve fitting of Fig. 4e, f, the θ_{SH} of Pt_3Sn and $Pt_3Sn_xFe_{1-x}$ is estimated to be 0.4 and 0.38, respectively. These values are larger than that of the Pt reference (θ_{SH} ~ 0.1) with the same experimental process and testing method (Fig. S11). Such high θ_{SH} could originate from the high spin Hall conductivity of the Pt_3Sn. A spin Hall conductivity up to ~$4.34\times10^5\,\hbar/2e\ (\Omega\cdot m)^{-1}$ for Pt_3Sn is predicted, which is two times larger than that of WSM WTe_2 (Fig. S12). We note that there is no significant difference of the SOT efficiency between Pt_3Sn and $Pt_3Sn_xFe_{1-x}$, which could possibly be due to the small change of the band structure between the two (more discussion in Supplementary Note 5).

Discussion

In this study, the high crystallinity, industrial-compatible topological semimetals, Pt_3Sn and $Pt_3Sn_xFe_{1-x}$, have been fabricated via the sputtering method for the advanced SOT devices. In combination with first-principles calculation and three-transistor model study, we thoroughly study the robust quadratic and linear NLMR features of Pt_3Sn and $Pt_3Sn_xFe_{1-x}$ thin films, which can not only extend the understanding of chiral anomaly in sputtered topological semimetal systems, but also demonstrate the feasibility to design and/or control the topological properties through seed layers or dopants. Meanwhile, the promising SOT performance of the Pt_3Sn and $Pt_3Sn_xFe_{1-x}$ thin films can inspire us to explore more novel topological semimetals for practicable spintronic applications.

Methods

Sample preparation and characterization

The Pt_3Sn and $Pt_3Sn_xFe_{1-x}$ samples studied in this work were prepared on single crystal (001) MgO substrates by magnetron sputtering under an ultrahigh vacuum (base pressure < 5.0×10^{-8} Torr). The Pt_3Sn thin films were deposited using $PtSn_4$ and Pt targets, and the $Pt_3Sn_xFe_{1-x}$ thin films are prepared using $PtSn_4$, Pt, and Fe targets with substrate temperature of 350 °C. The Pt thin film was also grown with the same experimental condition as a reference. The MgO (6.0 nm)/Ta (5.0 nm) capping layer was grown after the substrate was cooled down to room temperature. The pressure of Ar working gas is 2.1 mTorr for all the layers. The structural features of Pt_3Sn thin films were characterized by out-of-plane (θ–2θ scan) x-ray diffraction (XRD) with Co-Kα radiation (λ = 0.179 nm) using a Bruker D8 Discover system and by analytical electron microscopy using aberration-corrected FEI Titan G2 60-300 STEM equipped with super-X EDX detector. Cross-sectional samples

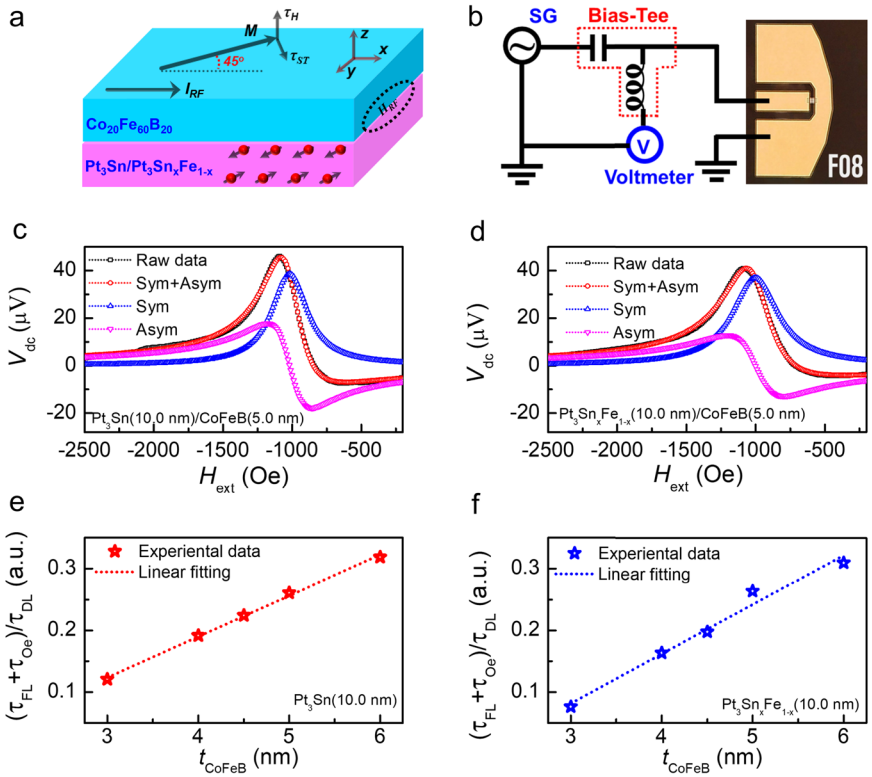

Fig. 4 | Spin torque efficiency. a, **b** The schematic of the ST-FMR measurement and experimental setup with the microscopy of the device. **c**, **d** the room-temperature ST-FMR spectra for the Pt_3Sn (10.0 nm)/CoFeB (5.0 nm) and $Pt_3Sn_xFe_{1-x}$ (10.0 nm)/CoFeB (5.0 nm) devices. **e**, **f** The ratio $(\tau_{FL} + \tau_{Oe})/\tau_{AD}$ plotted against the thickness of the CoFeB layer. Through the linear fitting, spin torque efficiencies θ_{SH} of ~0.4 and ~0.38 are obtained for Pt_3Sn (10.0 nm) and $Pt_3Sn_xFe_{1-x}$ (10.0 nm), respectively.

for the STEM study were prepared by using a FEI focused-ion beam (FIB) system. The Pt_3Sn and $Pt_3Sn_xFe_{1-x}$ samples were patterned into Hall bar devices by photolithography and Ar ion milling. And the electrical transport of Pt_3Sn and $Pt_3Sn_xFe_{1-x}$ Hall bar devices was tested through DC setup measurement by utilizing a Physical Property Measurement System (Quantum Design, DynaCool).

Device fabrication and electrical testing

The samples with the stack of MgO (001) sub./Pt_3Sn (60.0 nm)/MgO (6.0 nm)/Ta (5.0 nm), MgO (001) sub./Pt (Mo) (2.0 nm)/Pt_3Sn (60.0 nm)/MgO (6.0 nm)/Ta (5.0 nm), and MgO (001) sub./$Pt_3Sn_xFe_{1-x}$ (60.0 nm)/MgO (6.0 nm)/Ta (5.0 nm) (numbers indicate the thickness in nm, same below), were prepared and patterned into Hall bar devices with 4–12-μm width and 144-μm length using an optical lithography process. The electrode with Ti (10.0 nm)/Au (150.0 nm) was deposited by CHA evaporator after etching the MgO (6.0 nm)/Ta (5.0 nm). Then temperature-dependent magnetoresistance, resistance, and Hall effect were tested by a physical property measurement system (PPMS) with a dc setup with Keithley's 2182 nanovoltmeter and 6221 current source.

The Pt_3Sn (10.0 nm)/CoFeB (3.0–6.0 nm), Mo (2.0 nm)/Pt_3Sn (10.0 nm)/CoFeB (3.0–6.0 nm), $Pt_3Sn_xFe_{1-x}$ (10.0 nm)/CoFeB (3.0–6.0 nm) and Pt (5.0 nm)/CoFeB (3.0–6.0 nm) samples were patterned into rectangular-shaped microstrips with dimensions of 5–20-μm width and 30-μm length by optical lithography and Ar ion milling. The electrode with Ti (10.0 nm)/Au (150.0 nm) was deposited by CHA evaporator. Symmetric coplanar waveguides in the ground-signal-ground (GSG) form were utilized for microwave injection into the Pt_3Sn ($Pt_3Sn_xFe_{1-x}$)/CoFeB microstrips. A bias tee was used to inject microwave current and measure the resulting dc voltage at the same time. During the measurement, a microwave current with constant frequency (6–15 GHz) is injected while a magnetic field is swept at an angle of 45° with respect to the microstrips, and the output dc voltage is measured at each magnetic field with Keithley's 2182 nanovoltmeter.

DFT calculations

The total-energy electronic structure calculations were carried out using first-principles methods based on DFT. The generalized gradient approximation exchange-correlation potentials plus the projector augmented wave method for the electron-ion interaction was used[55], as implemented in Vienna ab initio simulation package code[56]. All self-consistent calculations were performed with a plane-wave cutoff of 500 eV. The geometric optimizations were carried out without any constraint until the force on each atom is less than 0.01 eV/A and the change of energy per cell is smaller than 10^{-5} eV. The Brillouin zone k-point sampling was set with a 21 × 21 × 21 Γ-centered Monkhorst-Pack grids. Wannier 90 package was used to fit the DFT band structures and calculate the SHC of Pt_3Sn alloys[57]. Fe doping is performed using the virtual crystal approximation method with a doping ratio of 5%, as suggested from experiments.

Data availability

The data that support the plots within this paper and other findings of this study are available from the corresponding author upon request.

References

1. Tang, F. et al. Comprehensive search for topological materials using symmetry indicators. *Nature* **566**, 486 (2019).
2. Zhang, T. et al. Catalogue of topological electronic materials. *Nature* **566**, 475 (2019).
3. Vergniory, M. G. et al. A complete catalogue of high-quality topological materials. *Nature* **566**, 480 (2019).
4. Hasan, M. Z. & Kane, C. L. Colloquium: topological insulators. *Rev. Mod. Phys.* **82**, 3045 (2010).

5. Qi, X.-L. & Zhang, S.-C. Topological insulators and superconductors. *Rev. Mod. Phys.* **83**, 1057 (2011).
6. Armitage, N. P., Mele, E. J. & Vishwanath, A. Weyl and Dirac semimetals in three-dimensional solids. *Rev. Mod. Phys.* **90**, 015001 (2018).
7. Mellnik, A. R. et al. Spin-transfer torque generated by a topological insulator. *Nature* **511**, 449 (2014).
8. Fan, Y. et al. Magnetization switching through giant spin-orbit torque in a magnetically doped topological insulator heterostructure. *Nat. Mater.* **13**, 699 (2014).
9. Han, J. et al. Room-temperature spin-orbit torque switching induced by a topological insulator. *Phys. Rev. Lett.* **119**, 077702 (2017).
10. DC, M. et al. Room-temperature high spin-orbit torque due to quantum confinement in sputtered $Bi_xSe_{(1-x)}$ films. *Nat. Mater.* **17**, 800 (2018).
11. Khang, N. H. D., Ueda, Y. & Hai, P. N. A conductive topological insulator with large spin Hall effect for ultralow power spin-orbit torque switching. *Nat. Mater.* **17**, 808 (2018).
12. Ramaswamy, R. et al. Spin orbit torque driven magnetization switching with sputtered Bi_2Se_3 spin current source. *J. Phys. D Appl. Phys.* **52**, 224001 (2019).
13. Liu, Z. et al. Discovery of a three-dimensional topological Dirac semimetal, Na_3Bi. *Science* **343**, 864 (2014).
14. Xu, S.-Y. et al. Discovery of a Weyl fermion semimetal and topological fermi arcs. *Science* **349**, 613 (2015).
15. Lv, B. Q. et al. Experimental discovery of Weyl semimetal TaAs. *Phys. Rev. X* **5**, 031013 (2015).
16. Lu, L. et al. Experimental observation of Weyl points. *Science* **349**, 622 (2015).
17. MacNeill, D. et al. Control of spin-orbit torques through crystal symmetry in WTe_2/ferromagnet bilayers. *Nat. Phys.* **13**, 300 (2017).
18. Li, P. et al. Spin-momentum locking and spin-orbit torques in magnetic nano-heterojunctions composed of Weyl semimetal WTe_2. *Nat. Commun.* **9**, 3990 (2018).
19. Shi, S. et al. All-electric magnetization switching and Dzyaloshinskii-Moriya interaction in WTe_2/ferromagnet heterostructures. *Nat. Nanotechnol.* **14**, 945 (2019).
20. Fan, Y. et al. Spin pumping and large field-like torque at room temperature in sputtered amorphous WTe_{2-x} films. *APL Mater.* **8**, 041102 (2020).
21. Xu, H. et al. High spin Hall conductivity in large-area type-II Dirac semimetal $PtTe_2$. *Adv. Mater.* **32**, 2000513 (2020).
22. Zhao, B. et al. Unconventional charge-spin conversion in Weyl-semimetal WTe_2. *Adv. Mater.* **32**, 2000818 (2020).
23. Li, X. et al. Large and robust charge-to-spin conversion in sputtered conductive WTe_x with disorder. *Matter* **4**, 1639 (2021).
24. Yanez, W. et al. Spin and charge interconversion in Dirac-Semimetal thin films. *Phys. Rev. Appl.* **16**, 054031 (2021).
25. Nielsen, H. B. & Ninomiya, M. The Adler-Bell-Jackiw anomaly and Weyl fermions in a crystal. *Phys. Lett. B* **130**, 389 (1983).
26. Kim, H.-J. et al. Dirac versus Weyl fermions in topological insulators: Adler-Bell-Jackiw anomaly in transport phenomena. *Phys. Rev. Lett.* **111**, 246603 (2013).
27. Xiong, J. et al. Evidence for the chiral anomaly in the Dirac semimetal Na_3Bi. *Science* **350**, 413 (2015).
28. Zhang, C.-L. et al. Signatures of the Adler-Bell-Jackiw chiral anomaly in a Weyl fermion semimetal. *Nat. Commun.* **7**, 10735 (2016).
29. Son, D. T. & Spivak, B. Z. Chiral anomaly and classical negative magnetoresistance of Weyl metals. *Phys. Rev. B* **88**, 104412 (2013).
30. Burkov, A. A. Negative longitudinal magnetoresistance in Dirac and Weyl metals. *Phys. Rev. B* **91**, 245157 (2015).
31. Sharma, G., Goswami, P. & Tewari, S. Chiral anomaly and longitudinal magnetotransport in type-II Weyl semimetals. *Phys. Rev. B* **96**, 045112 (2017).
32. Zyuzin, V. A. Magnetotransport of Weyl semimetals due to the chiral anomaly. *Phys. Rev. B* **95**, 245128 (2017).
33. Cortijo, A. Linear magnetochiral effect in Weyl semimetals. *Phys. Rev. B* **94**, 241105(R) (2016).
34. Ishizuka, H. & Nagaosa, N. Robustness of anomaly-related magnetoresistance in doped Weyl semimetals. *Phys. Rev. B* **99**, 115205 (2019).
35. Wang, Y. et al. Gate-tunable negative longitudinal magnetoresistance in the predicted type-II Weyl semimetal WTe_2. *Nat. Commun.* **7**, 13142 (2016).
36. Liang, T. et al. Anomalous Hall effect in $ZrTe_5$. *Nat. Phys.* **14**, 451 (2018).
37. Liang, T. et al. Ultrahigh mobility and giant magnetoresistance in the Dirac semimetal Cd_3As_2. *Nat. Mater.* **14**, 280 (2015).
38. Li, H. et al. Negative magnetoresistance in Dirac semimetal Cd_3As_2. *Nat. Commun.* **7**, 10301 (2016).
39. Arnold, F. et al. Negative magnetoresistance without well-defined chirality in the Weyl semimetal TaP. *Nat. Commun.* **7**, 11615 (2016).
40. Wiedmann, S. et al. Anisotropic and strong negative magnetoresistance in the three-dimensional topological insulator Bi_2Se_3. *Phys. Rev. B* **94**, 081302(R) (2016).
41. Shi, Q. et al. Colossal negative magnetoresistance in a two-dimensional electron gas. *Phys. Rev. B* **89**, 201301(R) (2014).
42. Alekseev, P. S. Negative magnetoresistance in viscous flow of two-dimensional electrons. *Phys. Rev. Lett.* **117**, 166601 (2016).
43. Breunig, O. et al. Gigantic negative magnetoresistance in the bulk of a disordered topological insulator. *Nat. Commun.* **8**, 15545 (2017).
44. Dai, X., Du, Z. Z. & Lu, H.-Z. Negative magnetoresistance without chiral anomaly in topological insulators. *Phys. Rev. Lett.* **119**, 166601 (2017).
45. Andreev, A. V. & Spivak, B. Z. Longitudinal negative magnetoresistance and magnetotransport phenomena in conventional and topological conductors. *Phys. Rev. Lett.* **120**, 026601 (2018).
46. Xu, J. et al. Negative longitudinal magnetoresistance in gallium arsenide quantum wells. *Nat. Commun.* **10**, 287 (2019).
47. Wu, Y. et al. Dirac node arcs in $PtSn_4$. *Nat. Phys.* **12**, 667 (2016).
48. Kim, M., Wang, C.-Z. & Ho, K.-M. Coexistence of type-II Dirac point and weak topological phase in Pt_3Sn. *Phys. Rev. B* **96**, 205107 (2017).
49. Zhou, J. et al. Intrinsic spin Hall conductivity of the semimetals $MoTe_2$ and WTe_2. *Phys. Rev. B* **99**, 060408(R) (2019).
50. Pippard, A. B. *Magnetoresistance In Metals* (Cambridge University Press, 2009).
51. Kharzeev, D. E. The Chiral magnetic effect and anomaly-induced transport. *Prog. Part. Nucl. Phys.* **75**, 133 (2014).
52. Gorbar, E. V., Miransky, V. A. & Shovkovy, I. A. Chiral anomaly, dimensional reduction, and magnetoresistivity of Weyl and Dirac semimetals. *Phys. Rev. B* **89**, 085126 (2014).
53. Li, H. et al. Determination of spin-orbit torques by thickness-dependent spin orbit torque FMR measurement. *arXiv* https://doi.org/10.48550/arXiv.2009.13162 (2020).
54. Pai, C.-F. et al. Dependence of the efficiency of spin Hall torque on the transparency of Pt/ferromagnetic layer interfaces. *Phys. Rev. B* **92**, 064426 (2015).
55. Perdew, J. P., Burke, K. & Ernzerhof, M. Generalized gradient approximation made simple. *Phys. Rev. Lett.* **77**, 3865 (1996).
56. Kresse, G. & Hafner, J. Ab initio molecular dynamics for liquid metals. *Phys. Rev. B* **47**, 558(R) (1993).
57. Pizzi, G. et al. Wannier90 as a community code: new features and applications. *J. Phys. Condens. Matter* **32**, 165902 (2020).

Acknowledgements

This project is supported by SMART, one of seven centers of nCORE, a Semiconductor Research Corporation program, sponsored by National

Institute of Standards and Technology (NIST). T.P. and D.Z. were partly supported by ASCENT, one of six centers of JUMP, a Semiconductor Research Corporation program that is sponsored by MARCO and DARPA. This work was partially supported by the UMN MRSEC program under award number DMR-2011401 (Seed). Parts of this work were carried out in the Characterization Facility of the University of Minnesota, which receives partial support from the NSF through the MRSEC (Award Number DMR-2011401). Portions of this work were conducted in the Minnesota Nano Center, which is supported by the National Science Foundation Nano Coordinated Infrastructure Network (NNCI) under Award Number ECCS-2025124. J.P.W. and D.Z. are grateful for the useful discussions with former Nanomagnetism and Quantum Spintronics group members at UMN: Dr. Mahendra D.C. and Dr. Lakhan Bainsla.

Author contributions

J.P.W. initialized and planned the project. D.Z. and J.P.W. conceived the experiments. D.Z. designed and prepared all the samples. W.J. and T.L. performed the DFT calculations and proposed the model. H.Y. and K.A.M. carried out STEM and EDX studies. D.Z., T.P, Z.C., G.Y., and J.G.B. carried out the XRD measurements. D.Z. and O.J.B. patterned the Hall Bar devices for ST-FMR measurement. D.Z. carried out the ST-FMR measurements with Y.F.; P.W.S. contributed to the discussion of the crystalline phase and the band structure of $PtSn_4$ and Pt_xSn_y materials in general. D.Z. and W.J. wrote the manuscript with J.P.W. and T.L. All the authors discussed the results and commented on the manuscript.

Competing interests

The authors declare no competing interests.

Additional information

Supplementary information The online version contains supplementary material available at https://doi.org/10.1038/s41467-023-39408-2.

Correspondence and requests for materials should be addressed to Delin Zhang, Tony Low or Jian-Ping Wang.

Peer review information *Nature Communications* thanks Xiufeng Han, Anlian Pan and the other, anonymous, reviewer(s) for their contribution to the peer review of this work.